AGU PUBLICATIONS

Radio Science

RESEARCH ARTICLE
10.1002/2016RS005951

Key Points:
- HF beacon network established in Peru for ionospheric specification
- Observables include group delay, Doppler shift, bearing, polarization, and power
- Numerical model for inverting multistatic beacon data developed

Correspondence to:
D. L. Hysell,
dlh37@cornell.edu

Citation:
Hysell, D. L., M. A. Milla, and J. Vierinen (2016), A multistatic HF beacon network for ionospheric specification in the Peruvian sector, *Radio Sci.*, *51*, doi:10.1002/2016RS005951.

Received 13 JAN 2016
Accepted 17 APR 2016
Accepted article online 23 APR 2016

A multistatic HF beacon network for ionospheric specification in the Peruvian sector

D. L. Hysell[1], M. A. Milla[2], and J. Vierinen[3]

[1]Earth and Atmospheric Sciences, Cornell University, Ithaca, New York, USA, [2]Jicamarca Radio Observatory, Lima, Peru, [3]Haystack Observatory, MIT, Westford, Massachusetts, USA

Abstract A small network of HF beacon transmitters and receivers has been deployed in Peru for specifying the *F* region ionosphere in the sector. The effort is motivated by ionospheric disturbances associated with equatorial spread *F* (ESF) and specifically disturbances arising under inauspicious conditions for ESF as determined by numerical simulations. The beacons operate at dual frequencies (2.72 and 3.64 MHz). They are CW but incorporate pseudorandom noise (PRN) coding so that the group delays of the links can be measured. Other observables are power, Doppler shift, bearing, and polarization. A transmitter is currently deployed at Ancon (11°46′37″S, 77°09′1″W, 51 m above sea level (asl)), while receivers are at Jicamarca (11°57′5.8″S, 76°52′27″W, 510 m asl) and Huancayo (12°02′30″S, 75°19′15″W, 3315 m asl). An algorithm for inverting the beacon data combined with electron density profiles from Jicamarca is described. Data and representative solutions from an experimental campaign held in August 2015 are presented and evaluated.

1. Introduction

The dominant space weather phenomena at low geomagnetic latitudes are disturbances in the *F* region ionosphere associated with equatorial spread *F* (ESF) conditions. These conditions are telltale of convective plasma instabilities driven by the free energy in the *F* region bottomside which becomes unstably stratified at sunset. The disturbances cause refraction, diffraction, and scattering of radio signals, interfere with communication, navigation, and imaging systems, and pose operational risks (see *Woodman* [2009] and *Kelley et al.* [2011] for reviews). We study ESF for the insights it gives into basic plasma physics as well as to mitigate the risks such as those stemming from positioning errors induced in Global Navigation Satellite Systems (GNSS) [e.g., *Kintner et al.*, 2007].

A three-dimensional numerical simulation code capable of reproducing the unstable background flow conditions in the postsunset equatorial *F* region was constructed to investigate whether ESF disturbances are sufficiently well understood for short-term forecasting. The simulation includes instabilities driven by vertical currents in the valley region which play a crucial role during the early stages of ESF [*Hysell and Kudeki*, 2004]. Data from the Jicamarca Radio Observatory near Lima, Peru, were used both to initialize and to drive the simulation. In a series of campaign studies, the simulation was able to recover (predict "after the fact") the presence or absence of ionospheric disturbances [*Hysell et al.*, 2014a, 2014b, 2015]. The simulation produced no false alarms, implying that no necessary condition for instability is being neglected in the simulations. On occasion, the simulation had missed detections, failing to anticipate disturbances that occurred under seemingly inauspicious conditions. Our surmise is that some of these unanticipated disturbances were not locally generated but instead propagated or advected into the region, being associated possibly with gravity waves or traveling ionospheric disturbances.

An HF beacon network is consequently being constructed to monitor the ionosphere around Jicamarca (rather than just the small volume directly overhead) to investigate the missed detections. Transmitting stations send PRN-coded HF CW signals at two frequencies. Receiving stations decode the signals and register their group delay, Doppler shift, and power. Other observables include the polarization and bearing of the received signal. This information is invertible and can be used to construct a regional model of the *F* region in the Peruvian sector. An algorithm capable of ingesting data from the beacons, the Jicamarca incoherent scatter radar (ISR), and other instruments is being developed and tested.

In this paper, the beacon network is described, and example data from a recent campaign at Jicamarca are shown. The algorithm for inverting the beacon data is also described and demonstrated. The network is a prototype at present, but there appear to be no serious impediments to building, operating, and obtaining ionospheric specifications from a much larger one.

2. Beacon Network Description

The main purpose of the beacon network is to expand the region where ionospheric disturbances can be monitored to help place the phenomena seen directly over Jicamarca in a regional context. Specifically, we seek to know more about ionospheric irregularities over Jicamarca during ESF events that are not predicted by the numerical simulations. Below, we describe the present state of the hardware and "software" involved.

2.1. Hardware

The hardware for our beacon transmitters and receivers is based on integrated software-defined transceivers. The transceivers combine two 100 MS/s capable, 14 bits analog to digital converters and a 400 MS/s, 16 bits digital to analog converter in a single, compact package. They utilize GPS-disciplined oscillators for absolute time synchronization. Throughput is as high as 25 MSPS (Million samples per second) of complex baseband signal.

A beacon transmitter station consists of two transceivers connected to separate inverted-V dipole antennas through small amplifier chains producing approximately 0.5 W of continuous wave power each. (In the future, the power will be increased to approximately 10 W to help overcome ionospheric absorption during the daytime, but 0.5 W is adequate for nighttime work.) The transmitting antennas are parallel to one another and aligned northwest to southeast. We use two transmitters to emit two HF frequencies — 2.72 and 3.64 MHz.

The transmitted waveform is a unique pseudorandom binary phase (PRN) code with a baud length of 10 μs and a repetition time of 100 ms. The code is transmitted continuously and affords compression ratios up to a factor of 10,000. We do not attempt to shape the emitted waveform with sidelobe-removing filters but instead analyze the received signal using a linear least squares filter in lieu of more standard matched filtering in order to suppress range sidelobes. Subsequent processing increases the processing gain to a factor of 1E6 for an echo occupying a single Doppler bin. Different transmitters send different codes.

For reception stations, a single two-channel transceiver, each channel capable of receiving two frequencies, is connected to a pair of short, wideband dipole antennas through chains of low-noise amplifiers. The receiving antennas are aligned northwest to southeast. Pairs of antennas can be used for interferometry. The interferometry baseline is 12 m long.

The received signal is sampled at a rate of 10 MS/s, shifted to an intermediate frequency between 2.72 and 3.64 MHz and then resampled at a rate of 1 MS/s. We mix to IF first in order to be able to monitor two widely spaced frequencies using a single hardware receiver channel. Subsequent decimation reduces the effective sample rate to 100 kS/s, giving a range resolution of 1.5 km. Estimates of the sample voltages in each range gate are formed every 100 ms, coherently processed for 10 s and then detected, producing range-Doppler maps. Spectra and cross spectra are not presently incoherently integrated for subsequent analysis. In the future, the overall cadence will likely be reduced from 10 s to something longer through incoherent integration to accommodate more stations and longer runs.

There is presently one transmitting station in Ancon (11°46′37″S, 77°09′1″W, 51 m above sea level (asl)), one receiving station at Jicamarca with dual receivers (11°57′5.8″S, 76°52′27″W, 510 m asl), and one receiving station in Huancayo (12°02′30″S, 75°19′15″W, 3315 m asl), Peru. (The Ancon-Jicamarca, Ancon-Huancayo, and Jicamarca-Huancayo stations are separated by about 36, 201, and 170 km, respectively.) The extra receiver at Jicamarca uses antennas aligned northeast to southwest, i.e., orthogonal to the other antennas. This makes it possible to measure the bearing and polarization of the incoming signal. Synchronization of the two receivers is by means of a common, GPS-disciplined clock and PPS timing signal.

2.2. Software — HF Data Inversion and Modeling

The HF beacon network probes the bottomside *F* region ionosphere in the region around Jicamarca, providing information about plasma density irregularities well outside the radar's field of view (that might eventually drift into the field of view). The advantage of the beacon network is that it can monitor a large volume of space for extended periods of time at low cost and with only minimal human intervention, infrastructure,

and impact. The disadvantage is that the observables are related to the ionospheric state in a complicated way. Like GPS signals, the beacon signals represent path-integrated quantities. Unlike GPS, the paths in this case are not straight lines and are unknown a priori. Furthermore, the HF beacon observables depend on parameters other than the plasma number density. Notably, the magnetic field and electron-neutral collision frequency appear in the forward model as well. Inverting the beacon data is challenging, but the computational resources required are now available. Below, the methodology used to model ionospheric electron densities from the beacon data is described.

Ray tracing. Each link in the beacon network provides up to five ionospheric observables related to the group delay, phase delay, power, bearing, and polarization of the ray that defines the link. The group delay comes from the absolute propagation delay time which is determined from processing the PRN code for the given link. This is perhaps the most important observable. The time rate of change of the phase delay is the Doppler shift of the beacon signal, which is also observed, and numerical integration gives the phase delay to within an additive constant. The power of the received signal is known within a multiplicative constant. The bearing of the received ray is measured, at least partially, through radar interferometry. Two or more interferometry baselines give complete information about the bearing, whereas a single baseline gives the direction cosine between that baseline and the incoming ray vector. Signal polarization is derived from crossed antenna pairs.

The discussion pertaining to rays above signals that this work is being conducted in the domain of geometric optics which is valid so long as the wavelength of the signal is small compared to the gradient length scale of the index of refraction in the medium. This assumption is valid for HF waves in the equatorial ionosphere prior to the onset of ESF and for a limited time after that.

The concept of geometric optics has its origins in antiquity, and Fermat's principle dates to the middle of the seventeenth century. The equations of geometric optics as a means of solving hyperbolic differential equations in a general way were worked out by Hamilton early in the nineteenth century, but appropriate descriptions of the Hamiltonian for waves traveling in the ionosphere were only made available by Edward Appleton, Sydney Chapman, and Henry Booker in the twentieth century. A thorough computational treatment of the ionospheric ray tracing problem was presented by *Jones and Stephenson* [1975] (JS) which is still up to date for all intents and purposes. The JS treatment built on formalism from *Haselgrove* [1954] and *Lighthill* [1965], and its treatment of losses was updated slightly by *Sen and Wyller* [1960]. JS accounts for rays propagating in an inhomogeneous, lossy, birefringent, and dispersive medium. In our work, we have borrowed the JS formalism wholesale and merely updated the numerics.

The equations of geometric optics in three spatial coordinates and in time are

$$\frac{\mathrm{d}\mathbf{r}}{d\tau} = \frac{\partial H}{\partial \mathbf{k}} \tag{1}$$

$$\frac{\mathrm{d}t}{\mathrm{d}\tau} = -\frac{\partial H}{\partial \omega} \tag{2}$$

$$\frac{\mathrm{d}\mathbf{k}}{\mathrm{d}\tau} = -\frac{\partial H}{\partial \mathbf{r}} \tag{3}$$

$$\frac{\mathrm{d}\omega}{\mathrm{d}\tau} = \frac{\partial H}{\partial t} \tag{4}$$

where **r** is the physical coordinate of a point on the ray, **k** is the wave vector (wave normal, normalized to satisfy the dispersion relation), τ is a scale parameter which depends on the form of H, ω is the wave frequency, and t is time. In the above, the frequency and wave vector are characteristics of the wave, whereas background ionospheric parameters vary in space and time.

For the particular form of the Hamiltonian, any invariant quantity along the path of the ray may be used. For the JS procedure, H is taken to be either the real part of the Appleton-Hartree formula (or a variant thereof) or the real part of the Booker Quartic, depending on the proximity to the ray turning point. The independent variable for numerical integration is the accumulated group path length, which automatically becomes more granular near the turning point where the calculations are the most critical. For each case, *Jones and Stephenson* [1975] give the explicit system of equations to be integrated in a spherical coordinate system, obviating the need

for evaluating derivatives with finite differences. Additionally, ionospheric density, electron-neutral collision frequency, and magnetic field parameters must be supplied from one or another kind of ancillary model. We use the NRLMSISE-00 model as a basis for estimating electron-neutral collision frequencies and the latest International Geomagnetic Reference Field model for the geomagnetic field.

Our main innovation has been to upgrade the method for numerical integration from the original Runge-Kutta scheme used by JS. Originally, we tried a high-order Runge-Kutta-Fehlberg method, but while this was an improvement, the accuracy was inadequate for our purposes, the results being occasional instability in the shooting method described below. We eventually implemented a high-order Adams multistep method as described by *Shampine and Gordon* [1975]. The Adams method differs from single-step quadrature methods by making use of results from previous calculations made along a path. Despite its vintage, this method still represents the state of the art in numerical integration of nonstiff ordinary differential equations (ODEs).

Upon completion of the numerical integration of the system of first-order ODEs, one is left with the coordinates of a raypath for the *X*- or *O*-mode signal along with the associated group delay, phase delay, bearing (at the termination point), and also an estimate of the total attenuation along the path. These are the observables.

Shooting. The high-accuracy requirement for the ray tracing calculation described above stems from the fact that ray tracing is only the inner loop of a three-loop calculation. Ray tracing solves the initial value problem of finding where a ray originating from a given location with some azimuth, elevation, and frequency will terminate. For this project, we are interested specifically in rays that originate at a beacon transmitter and terminate at a receiver. This is not an initial value problem but a boundary value problem. It is solved with a shooting method (see, e.g., *Press et al.* [1988] for discussion). Shooting constitutes the middle loop of the overall inverse method.

In our method, a ray is launched from a transmit site with an initial guess for its azimuth and elevation. The discrepancy between the termination point of the ray and the receiver location is noted, and the azimuth and elevation are updated. The process is not unlike directing artillery fire (hence shooting). The procedure progresses iteratively until the boundary value problem is solved. At this point, the algorithm is able to predict the group delay, phase delay, relative power, and bearing of the signal at the receiver for a given beacon link for a candidate ionosphere. The algorithm used to optimizing the solution is the Levenberg Marquardt routine contained in the NETLIB repository. We find that tolerances of one part in 10^{11} are required in the ray tracing loop to achieve tolerances of one part in 10^6 in the shooting loop. This, in turn, permits tolerances of one part in 10^5 in the outer regularization loop which is described below.

A potential problem involves the possibility of integrating rays as their zenith angles cross the Spitze angle [see, e.g., *Budden*, 1988]. At this point, the dispersion relation for the *O* mode becomes multivalued. The rays for the Ancon-Jicamarca link, which is quasi-vertical, cross the Spitze angle, but the numerical integration never pursued the *Z*-mode solution instead of the *O* mode. The finite step size of the integrator was evidently wide enough to avoid this complication. In the future and under different ionospheric conditions, it may be necessary to compel the numerical integration to jump across the Spitze angle.

Regularized model. The aforementioned shooting loop, which is executed for every beacon link, requires a regional specification of the ionospheric number density, the quantity we are attempting to determine. This amounts to a classic inverse method—one that is strongly underdetermined. In order to reduce the size of the solution space (to a finite, tractable size), we parametrize the ionospheric density in the Andean region in terms of a number of discrete variables. We presume that the density profile can be described well in altitude h by a three-parameter Chapman function, i.e.,

$$n_e(h, n_\circ; h_m, h_\circ) = n_\circ \exp\left(1.0 - z - \exp(-z)\right) \tag{5}$$

$$z = \frac{h - h_m}{h_\circ} \tag{6}$$

which is usually a good assumption in the bottomside around twilight [e.g., *Anderson et al.*, 1987]. In the horizontal dimension, the parameters $n_\circ$, h_m, and $h_\circ$ are set through interpolation using bicubic B-splines which are 2-D generalizations of ordinary cubic B-splines [e.g., *De-Boor*, 1978]. B-splines or basis splines have a number of useful properties which make them suitable for basis functions. Cubic B-splines are continuous at least through their second derivatives at all points. They offer local support, such that the value in some region is

entirely controlled by the closest control points. B-splines are also variation diminishing and do not promote spurious oscillation.

Presently, we locate the B-spline knots on a uniform 15×15 grid at which the Chapman function parameters are specified. This means that the entire regional ionosphere is specified by 675 discrete parameters. This number is arbitrary and can be increased as the need arises, with attendant computational costs. Incorporating altitude profiles with more than three parameters could also be done trivially in the future if necessary.

The outer loop of the analysis then involves modifying the 675 parameters iteratively to minimize the discrepancy between predictions and observations. Presently, observations include the group delays for all the links in the beacon network in addition to ionospheric density profiles from either the ionosonde at Jicamarca or the incoherent scatter radar itself when data are available. Minimization is done using the Levenberg Marquardt routine contained in the NETLIB repository once again.

Since the model is underdetermined, regularization (damping) is incorporated in the iteration. Regularization techniques generally consider both the χ^2 data prediction error along with some measure of the regularity of the model, e.g., a norm of the model coefficients, their gradient, or their curvature. They proceed by (a) minimizing χ^2 while constraining the model norm, (b) minimizing the model norm while constraining χ^2, or (c) minimizing a weighted sum of the model norm and χ^2. The three approaches produce the same results given the appropriate choice of regularization parameter. In our case, we minimize the weighted sum of χ^2 and the model curvature, where the weight is the regularization parameter. The parameter is set so as to make χ^2 comparable to its estimated value. In this way, the method finds the ionospheric parameters which are consistent with the observations while exhibiting minimal structure. Thus, only features with support in the observations will be produced by the method.

The overall method is repeated for different time steps, providing a continuous regional specification of ionospheric plasma density in space and time. The solution from the previous time step provides an excellent initial guess for the current time step, expediting the required computations.

3. Example Campaign Data

For this study, we examine data from an unusual ESF event on 25/26 August 2015 observed during an observing campaign at Jicamarca. For a complete description of the experimental mode, see *Hysell et al.* [2014a]. On this day, the $F_{10.7}$ solar flux index was 123.9, and *Kp* varied between 1.0 and 2.7.

A combination of incoherent and coherent scatter observations is presented in Figure 1. Figure 1 (top left) shows plasma number densities derived from the backscatter power and normalized using Faraday rotation. Coherent scatter from ESF plasma density irregularities has been removed from the panel, leaving behind white space when and where it occurred. The panel immediately to the right shows an electron number density profile for 2345 UT (1845 LT) (solid line) together with a profile derived from the Parameterized Ionospheric Model or PIM model (dashed line) [*Daniell et al.*, 1995]. In previous studies, we have found that PIM can generally be made to reproduce actual conditions over Jicamarca around sunset by setting the $F_{10.7}$ solar flux parameter appropriately. Here it has been set to 150. PIM provides initial conditions for the aforementioned numerical simulations.

The next panel to the right shows zonal plasma drifts inferred from incoherent scatter. Normally, the drifts are eastward near and above the *F* peak during the times shown. In this case, the drifts were mainly westward between 0000 UT (1900 LT) and 0200 UT (2100 LT). Flow reversals like those depicted here occur frequently during disturbed conditions but very seldom during quiet times. The flow in evidence here is most atypical.

Figure 1 (top right) shows vertical plasma drifts. The superimposed plotter symbols indicate the altitude-averaged drifts. The drifts here are characterized by a small prereversal enhancement peaking at about 2330 UT (1830 LT), an early reversal at about 0100 UT (2000 LT), and a deep negative well thereafter. Such behavior is inauspicious for ESF plumes [e.g., *Stolle et al.*, 2008; *Kil et al.*, 2009; *Huang and Hairston*, 2015].

Figure 1 (bottom left) shows a zonal plasma drift profile for 2345 UT (1845 LT) (curve with error bars) together with a model profile generated using the aforementioned simulation code. For the simulation, thermospheric winds from the HWM-14 model were incorporated [*Drob et al.*, 2015]. Unlike the cases we have examined previously, the agreement is very poor here and cannot be rectified by simply scaling the model winds. The neutral and ionized gas circulation evidently differed drastically from the climatological average.

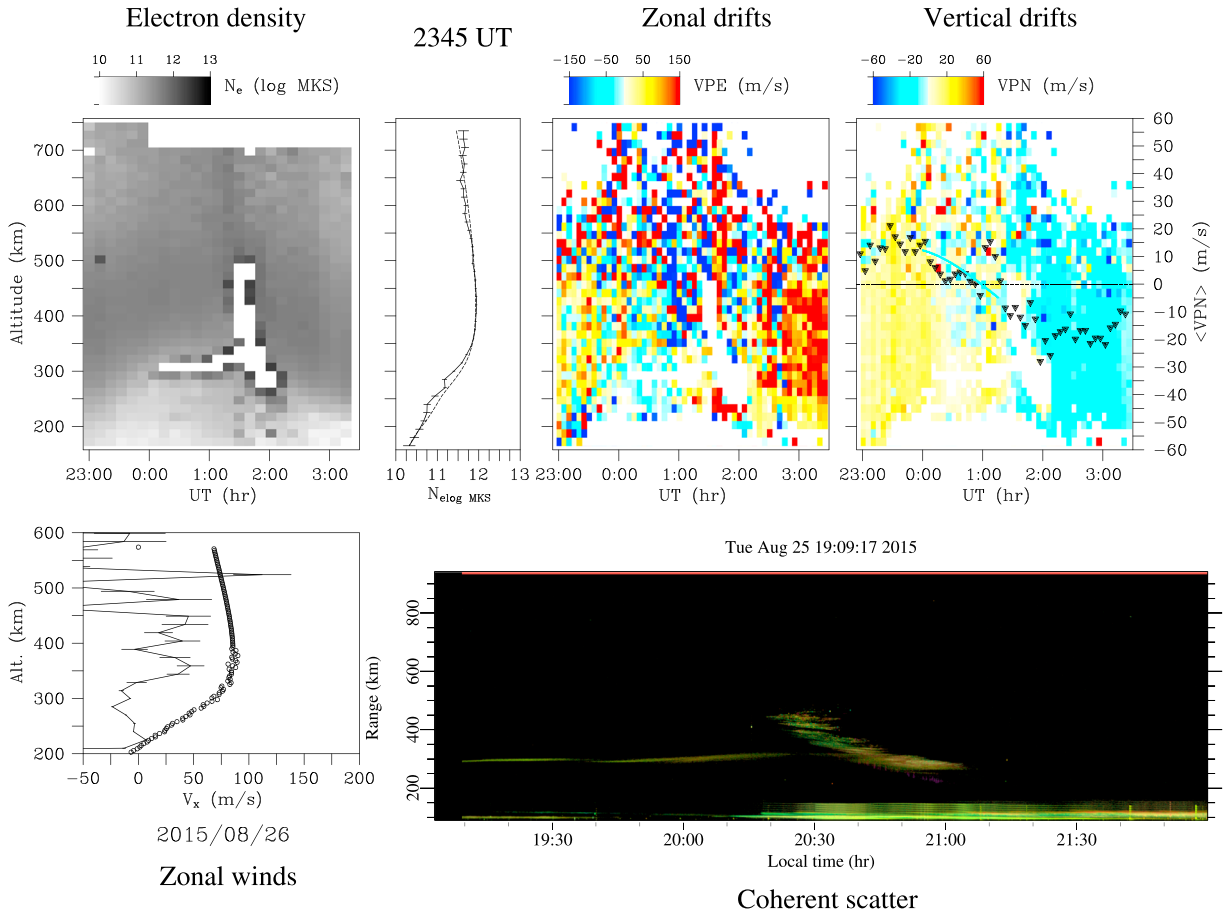

Figure 1. Jicamarca observations of ESF 25/26 August 2015. (top row) From left to right: electron density, electron density profiles at 2345 UT, zonal plasma drifts, and vertical plasma drifts. (bottom left) Measured zonal plasma drift profiles at 2345 UT (solid line with error bars) together with the computed drift profile (plotted points) at the start of the numerical simulation. (bottom right) Coherent backscatter. Note that UT = LT + 5 h.

Finally, Figure 1 (bottom right) shows coherent scatter observations from Jicamarca in range-time-intensity format. The coherent scatter was exceptionally weak during this event. Barely visible in the figure, which presents the signal-to-noise ratio of the echoes on a scale from −3 to 27 dB, is a bottom-type layer from 1900 to 2045 LT followed by a minor radar plume which passed overhead at about 2030 LT.

We have insufficient information about the thermospheric winds, which evidently departed drastically from the climatological average, to carry out an accurate numerical simulation of the events of 25 August 2015. However, a simulation performed using the climatological winds from HWM-14 predicted the bottom-type irregularity layer observed at ~300 km but not the radar plume. The weak prereversal enhancement and early reversal of the zonal electric field were prohibitive to local irregularity generation.

Sample data from the HF beacon links between Ancon and Jicamarca acquired during the same campaign are presented in Figure 2. The figure shows echoes plotted against group delay ($c\tau/2$) and local time. The intensity of the pixels indicates the signal-to-noise ratio, and the hue indicates Doppler shift. Information about the received ray bearing derived from interferometry and also the polarization is available but not plotted.

Despite the low power of the link, reflections from four hops are clearly recognizable. Multimode propagation is evident briefly before about 18 LT but not later. A single ESF plume passed through the region at about 2030 LT, giving rise to multiple satellite traces. These traces are visible for about a half hour prior to and after the passage of the plume. Outside of those times, the main echoes are distinct. There is no signature of the bottom-type layer from Figure 1, the reflection heights for the HF signals being below the layer height. White plotter symbols show the group delay of the first *F* region hop. At present, we use just this information (for all the links) in subsequent model analysis.

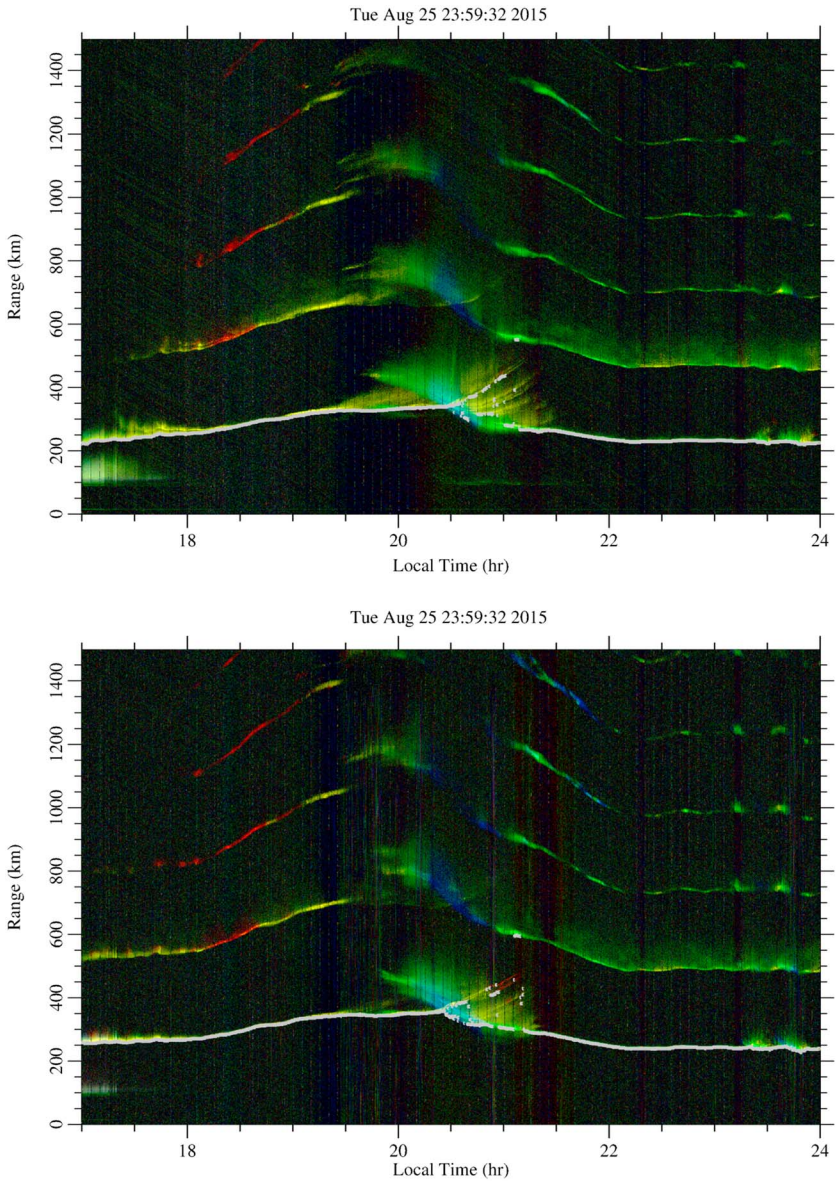

Figure 2. Beacon data for the Ancon-Jicamarca link for 25 August 2015. The (top) 2.72 MHz and (bottom) 3.64 MHz links. Echoes are sorted by group delay (range = $c\tau/2$) and local time. The intensity of the pixels indicates the SNR, and the color represents the Doppler shift. White plotter symbols identify the group delay of the first *F* layer hop. Red, green, and blue hues denote the signal-to-noise ratio (in the range −10–20 dB) in the −0.1, 0.0, and 0.1 Hz Doppler frequency bins, respectively.

Similar data are available for the Ancon-Huancayo link, although the signals are considerably weaker. Only the first hops are visible in those data. The signals are adequately strong for continuous estimates of the group delays.

4. Ionospheric Specification

Group delay estimates for all four links have been combined with ISR-derived density profiles from Jicamarca and modeled according to the methodology described in section 2. The results for the observations at 25 August 2015 are shown in Figure 3. Six panels depict results for six local times prior to the passage of the radar plume. (Results like these are available at 10 s intervals, but variations between successive results are gradual.) Quasi-isodensity contours for $n_e = 5 \times 10^4$ cm^3 and $n_e = 5 \times 10^5$ cm^3 are indicated in each panel by the green and cyan surfaces, respectively. The isodensity surfaces are found to be nearly horizontal planes in

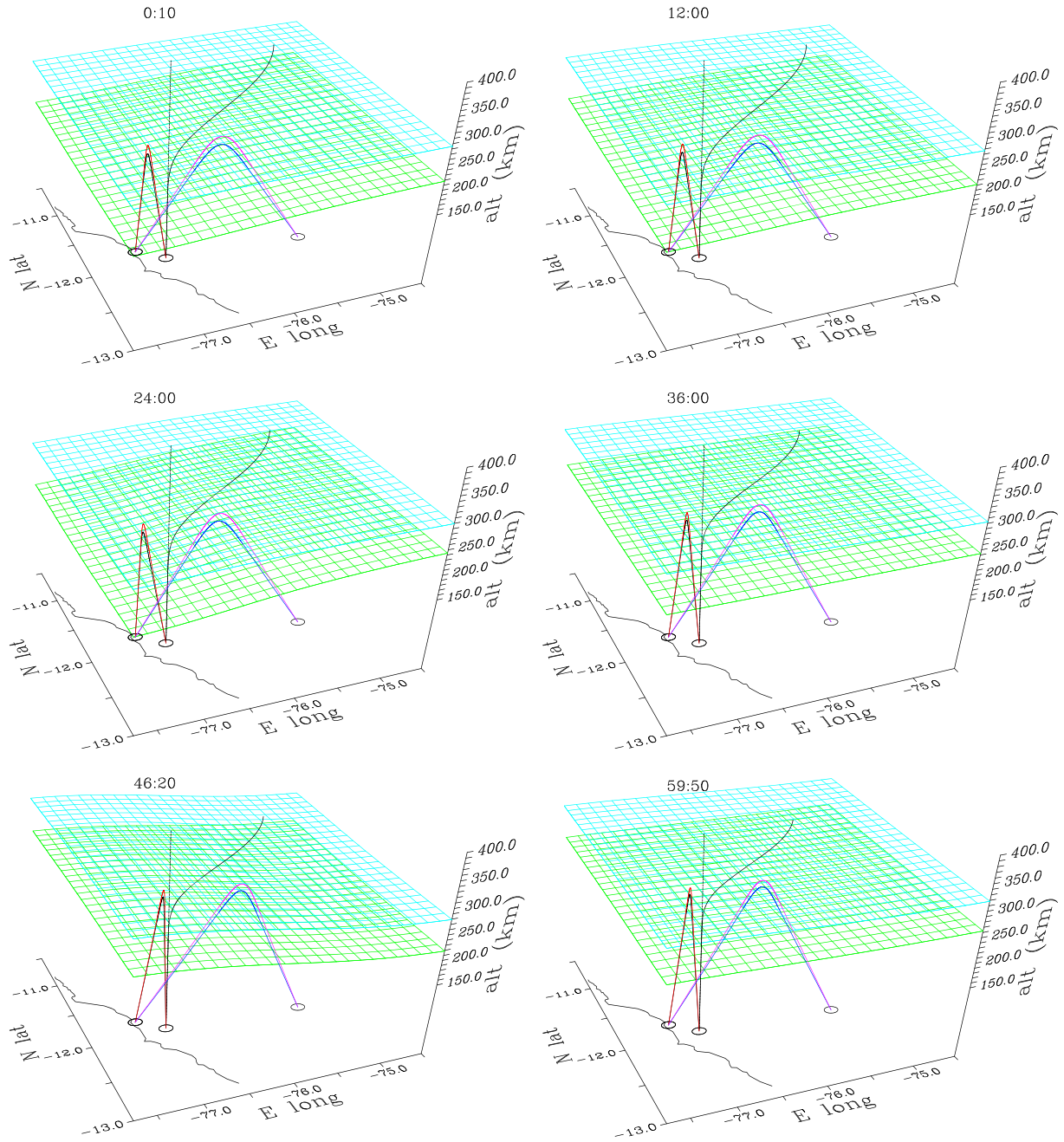

Figure 3. Ionospheric reconstructions based on beacon and ISR data. The six panels correspond to four different local times, as indicated. The ragged line in each panel is the Pacific coastline. The plotted surfaces are two isodensity contours. The black profile is the model density profile evaluated over Jicamarca. The four rays represent the four HF beacon links. The underlying ionospheric model is consistent with all available data at the given time.

the interval shown. In order to emphasize differences from pure horizontal stratification, the surfaces actually show the average height plus the deviation from the average multiplied by a factor of 5.

The ionospheric reconstruction captures the gradual postsunset ascent of the *F* layer over time as well as the east-west ionospheric tilt that follows the passage of the solar terminator. The standard deviation of the altitudes across the isodensity surfaces is of the order of 1 km throughout the first half of the interval examined but peaks at about 6 km toward the end. Animated sequences of figures like those in Figure 3 also suggest subtle ionospheric structuring at the spatial and temporal scales being analyzed. The number of links is too few to specify whether features are propagating or advecting through the region, however.

Significantly, perturbations in the group delays of the four links are accounted for by the model not through wholesale layer ascent and descent but instead mainly through layer tilts. A tilted ionosphere forces the rays to propagate away from great circle paths. Very subtle tilts can induce significant changes in group delay this way. It is therefore incorrect to interpret group delay as a proxy measurement for layer height at the reflection point. The modeled layer height barely changes on time scales during which the measured group delays vary significantly.

5. Summary and Future Work

A small network of dual-frequency HF beacons has been deployed in Peru to investigate disturbances in the *F* region ionosphere. We are particularly interested in getting contextual information about ESF events which occur under inauspicious conditions to complement observations made at Jicamarca.

The most important observable from the network is the group delay of the links which is obtained from the PRN coding of the CW HF signals. This information has been combined with measurements of the electron density profile at Jicamarca in a regional ionospheric specification model. The model finds the *F* region ionosphere which is consistent with all the available measurements while having minimum curvature in the horizontal directions.

Beacon data and ionospheric inversions from a campaign held in August 2015 have been presented and described. While the inversion problem is computationally expensive, it is tractable and stable. At present, however, the ionospheric specification is too coarsely resolved in space to offer much insight into the missed detection problem. It seems clear that the methodology is very sensitive to small tilts in the ionospheric layer that could help indicate the presence of disturbances propagating or advecting into the region over Jicamarca once the spatial resolution of the method is improved.

A number of improvements can be made to the network. First, the number of stations can be increased. For any given number of stations, the number of links is maximized when the stations are equally divided between transmitters and receivers and grows as the square of the number of stations. The number of links is increased further if every station can transmit and receive simultaneously. This modality should be possible given the low transmit power levels and the high dynamic range of the digital receivers.

In the future, it should also be possible to utilize more of the observables in the data inversion. The ray tracing code predicts the phase delay, power, and bearing of the received *O*- and *X*-mode signals already. Measured Doppler shifts prescribe the time rate of change of the phase delay from one time step to the next. Discrepancies between the observables and the model prescriptions can readily be added to the objective function used in the outer loop of the inverse method.

Still, other observables are available from the HF signals, although their utility to the project is less certain and requires investigation. It should be possible to observe the Faraday rotation of the signals received at Jicamarca. This is another indication of the line-integrated electron number density. Like the phase delay, the Faraday angle is a modulo-two-pi quantity that is best used to constrain the time evolution of the ionosphere. Both the Faraday angle and the phase delay are continuous quantities, unlike the group delay which is quantized at the level of the range resolution of the beacon system. The precision is therefore potentially greater.

A number of improvements to the data inversion method are also possible. One is the generalization of the altitude model to include both an *E* region and *F* region Chapman layer. Such a model would be better at representing the plasma density in the valley region where the density can be uniform over broad altitude spans. Another is parallelization, which will be necessary as the number of links is increased. As each link can be traced individually, parallelization should be efficient.

Validation of the network and the ionospheric specification method will be through a generalized cross-validation approach whereby, one by one, the sources of data are withdrawn from the inversion process and predicted independently by it. An overall model prediction error norm can be assembled by adding the error norms for each data source. That norm will, in turn, be used to optimize our regularization parameter. At present, we lack the data necessary for meaningful cross validation because we require all available data to construct our minimalist model. No other data sets capable of specifying the bottomside equatorial ionosphere in the immediate vicinity of Jicamarca are available presently.

Finally, it should be noted that the beacon network could be used as a ground-based alternative to GNSS. Given an ionospheric specification, it should be possible to determine the location of a beacon receiver based on the group delays of signals from three or more beacon transmitters. Incorporating topographic information reduces the number to two and should improve the solution given any number of received signals. Eventually, the coefficients that specify the ionospheric model could be determined in real time and transmitted by one of the beacons.

Acknowledgments
This work was supported by award FA9550-12-1-0462 from the Air Force Office of Scientific Research to Cornell University. The Jicamarca Radio Observatory is a facility of the Instituto Geofisíco del Perú operated with support from NSF award AGS-1433968 through Cornell. The help of the staff is much appreciated. Data used for this publication are available through the Madrigal database.

References

Anderson, D. N., M. Mendillo, and B. Herniter (1987), A semi-empirical low-latitude ionospheric model, *Radio Sci.*, *22*, 292–306.
Budden, K. G. (1988), *The Propagation of Radio Waves*, Cambridge Univ. Press, New York.
Daniell, R. E., L. D. Brown, D. N. Anderson, M. W. Fox, P. H. Doherty, D. T. Decker, J. J. Sojka, and R. W. Schunk (1995), Parameterized ionospheric model: A global ionospheric parameterization based on first principles models, *Radio Sci.*, *30*, 1499–1510.
De-Boor, C. (1978), *A Practical Guide to Splines*, Springer, New York.
Drob, D. P., et al. (2015), An update to the Horizontal Wind Model (HWM): The quiet time thermosphere, *Earth Space Sci.*, *2*, 301–319, doi:10.1002/2014EA000089.
Haselgrove, J. (1954), Report of conference on the physics of the ionosphere, *Tech. Rep.*, p. 355, Phys. Soc., London.
Huang, C. S., and M. R. Hairston (2015), The postsunset vertical plasma drift and its effects on the generation of equatorial plasma bubbles observed by the C/NOFS satellite, *J. Geophys. Res. Space Physics*, *120*, 2263–2275, doi:10.1002/2014JA020735.
Hysell, D. L., and E. Kudeki (2004), Collisional shear instability in the equatorial *F* region ionosphere, *J. Geophys. Res.*, *109*, A11301, doi:10.1029/2004JA010636.
Hysell, D. L., R. Jafari, M. A. Milla, and J. W. Meriwether (2014a), Data-driven numerical simulations of equatorial spread F in the Peruvian sector, *J. Geophys. Res. Space Physics*, *119*, 3815–3827, doi:10.1002/2014JA019889.
Hysell, D. L., M. A. Milla, L. Condori, and J. W. Meriwether (2014b), Data-driven numerical simulations of equatorial spread F in the Peruvian sector: 2. Autumnal equinox, *J. Geophys. Res. Space Physics*, *119*, 6981–6993, doi:10.1002/2014JA020345.
Hysell, D. L., M. A. Milla, L. Condori, and J. Vierinen (2015), Data-driven numerical simulations of equatorial spread *F* in the Peruvian sector. 3: Solstice, *J. Geophys. Res. Space Physics*, *120*, 10,809–10,822, doi:10.1002/2015JA021877.
Jones, R. M., and J. J. Stephenson (1975), A versatile three-dimensional ray tracing computer program for radio waves in the ionosphere, *Tech. Rep. 75-76*, U.S. Dep. of Commer., Washington, D. C.
Kelley, M. C., J. J. Makela, O. de la Beaujardiere, and J. Retterer (2011), Convective ionospheric storms: A review, *Rev. Geophys.*, *49*, RG2003, doi:10.1029/2010RG000340.
Kil, H., L. J. Paxton, and S. J. Oh (2009), Global bubble distribution seen from ROCSAT-1 and its association with the evening prereversal enhancement, *J. Geophys. Res.*, *114*, A06307, doi:10.1029/2008JA013672.
Kintner, P. M., B. M. Ledvina, and E. R. de Paula (2007), GPS and ionospheric scintillations, *Space Weather*, *5*, S09003, doi:10.1029/2006SW000260.
Lighthill, M. J. (1965), Group velocity, *J. Inst. Math. Appl.*, *1*, 1–28.
Press, W. H., B. P. Flannery, S. A. Teukolsky, and W. T. Vetterling (1988), *Numerical Recipes in C*, Cambridge Univ. Press, New York.
Sen, H. K., and A. A. Wyller (1960), On the generalization of the Appleton-Hartree magnetoionic formulas, *J. Geophys. Res.*, *65*, 3931–3950.
Shampine, L. F., and M. K. Gordon (1975), *Computer Solution of Ordinary Differential Equations: The Initial Value Problem*, W. H. Freeman, San Francisco, Calif.
Stolle, C., H. Lühr, and B. G. Fejer (2008), Relation between the occurrence rate of ESF and the equatorial vertical plasma drift velocity at sunset derived from global observations, *Ann. Geophys.*, *26*, 3979–3988.
Woodman, R. F. (2009), Spread *F* — An old equatorial aeronomy problem finally resolved?, *Ann. Geophys.*, *27*, 1915–934.